Averaged implicit hydrodynamic model of semiflexible filaments

Preethi L. Chandran and Mohammad R. K. Mofrad[*]

Molecular Cell Biomechanics Laboratory, Department of Bioengineering, University of California, Berkeley, California 94720, USA

We introduce a method to incorporate hydrodynamic interaction in a model of semiflexible filament dynamics. Hydrodynamic screening and other hydrodynamic interaction effects lead to nonuniform drag along even a rigid filament, and cause bending fluctuations in semiflexible filaments, in addition to the nonuniform Brownian forces. We develop our hydrodynamics model from a string-of-beads idealization of filaments, and capture hydrodynamic interaction by Stokes superposition of the solvent flow around beads. However, instead of the commonly used first-order Stokes superposition, we do an equivalent of infinite-order superposition by solving for the true relative velocity or hydrodynamic velocity of the beads implicitly. We also avoid the computational cost of the string-of-beads idealization by assuming a single normal, parallel and angular hydrodynamic velocity over sections of beads, excluding the beads at the filament ends. We do not include the end beads in the averaging and solve for them separately instead, in order to better resolve the drag profiles along the filament. A large part of the hydrodynamic drag is typically concentrated at the filament ends. The averaged implicit hydrodynamics methods can be easily incorporated into a string-of-rods idealization of semiflexible filaments that was developed earlier by the authors. The earlier model was used to solve the Brownian dynamics of semiflexible filaments, but without hydrodynamic interactions incorporated. We validate our current model at each stage of development, and reproduce experimental observations on the mean-squared displacement of fluctuating actin filaments . We also show how hydrodynamic interaction confines a fluctuating actin filament between two stationary lateral filaments. Finally, preliminary examinations suggest that a large part of the observed velocity in the interior segments of a fluctuating filament can be attributed to induced solvent flow or hydrodynamic screening.

I. INTRODUCTION

Hydrodynamic interaction refers to the force communication between two particles mediated via the solvent. The motion of a particle causes a solvent flow around it, which in turn exerts a drag on a neighboring particle. This drag force on a particle from the solvent flow induced by a neighboring particle is referred to as hydrodynamic force.

Semiflexible filaments are polymers whose contour lengths are on scale of their persistence length, so that their thermally driven bending fluctuations are resisted by their elastic bending stiffness [1,2]. Semiflexible filaments make up the structural scaffold of cell and tissue matrices (actin and microtubules in cells, collagen in tissue), and understanding their dynamic behavior is critical to understanding force transmission and remodeling in cell and tissue matrices.

A semiflexible filament is subject to hydrodynamic forces due to solvent flows induced by the bending and diffusive motions both within itself and from its neighbors. However, dynamic models of semiflexible filaments typically neglect the drag forces arising from the induced solvent flow. For instance, consider a single semiflexible filament in dilute solution. Typical dynamic models assume the friction coefficient to be uniform along the filament length, and equal to

that of a unit rigid cylinder of same diameter [2–6]. However, Lagamarsino *et al.* [7] showed that when a rigid filament is modeled as a string-of-beads and the hydrodynamic interaction between beads accounted for, the drag force and friction coefficient along the filament is not uniform even when under a uniform force. The drag force is much greater at the beads toward the filament ends, and decreases at the beads toward the filament center [7]. While such nonuniform drag might not affect the overall motion of a rigid filament under uniform force, it will cause a semiflexible filament to bend under uniform force-a phenomenon that will be missed by semiflexible filament models assuming constant friction coefficient.

The nonuniform drag along a rigid filament is due to hydrodynamic screening. The solvent flow induced by the motion of the filament ends carry the central region of the filament with it. Since the central region is now partly drifting in the induced solvent flow, the relative velocity (observed velocity minus solvent velocity), and therefore drag experienced by it, is reduced. The phenomenon is akin to drafting in bicycle or car racing.

The observations of nonuniform drag due to hydrodynamic screening and other hydrodynamic interaction effects suggest that a part of the bending fluctuations of a semiflexible filament may be caused by the nonuniform drag, in addition to the nonuniform Browian forces. Therefore, a model of semiflexible filament dynamics that is used to interpret experimental observation needs to include the effects of hydrodynamic interaction, originating from within itself and from neighboring filaments.

The common approaches to capturing hydrodynamic interaction in rigid cylinders tend to employ two conceptual

———

*Corresponding author. Present address: Department of Bioengineering, University of California Berkeley 208A Stanley Hall #1762 Berkeley, CA 94720-1762; FAX: (510) 642-5835; mofrad@berkeley.edu

ideas. The first is to idealize the cylinder as a string of beads [8,9], and the second is to determine the hydrodynamic interaction between the beads by first-order superposition of Stokesian solvent fields [10]. Idealizing a filament as a string of beads has the advantages that the solvent flow equations around a moving bead are well established and that the geometry between interacting beads is relatively easy to handle. The chief disadvantage, however, is that solving for all beads in a string-of-beads approach makes it computationally expensive to model even a single filament [9]. Now consider the second idea. Stokesian dynamics is commonly used to describe solvent flow in these settings because of the small particle diameters and small velocities involved [11]. Stokesian flow equations are linear. Therefore the solvent velocity at any point in an assembly of beads can be estimated, to first order, by summing the solvent flows due to the motion of each bead alone. The hydrodynamic drag on a bead can then be determined from its observed velocity relative to the solvent velocity at its center. The first-order superposition approach to approximating induced solvent flow has the advantage that it is relatively simple to implement. However the disadvantage is that it neglects the reflection of the induced solvent flow between the beads, a higher-order superposition effect. As a result, the first-order superposition overlooks the hydrodynamic influence from neighboring particles which are stationary, and overestimates the hydrodynamic influence from neighboring particles that are drifting.

The aim of this paper is to introduce a method for including hydrodynamic interaction effects on a fluctuating semiflexible filament. The proposed method is still based on the two conceptual ideas discussed above and therefore retains their advantages. But it avoids the disadvantages associated with them: We retain the underlying ideas of idealizing the filament as a string of beads and of determining the hydrodynamic drag on the beads by Stokes superposition of the solvent fields around each bead. However instead of a first-order superposition, we do an infinite-order superposition by casting the relative velocity of a bead (observed velocity minus solvent velocity at bead center) as a separate variable and solving for it *implicitly*. We call the relative velocity of the bead as its hydrodynamic velocity, because the hydrodynamic drag on the bead is proportional to this relative velocity. The one-step implicit solution is equivalent to superposing many back and forth reflections of the solvent velocity fields, and therefore eliminates the errors of first-order Stokesian superposition. We then reduce the computation cost associated with the string-of-beads idealization by grouping all but the end beads into sections, and assuming uniform translational and rotational velocities for each section. This reduces the number of variables and equations to be solved. In grouping the velocities of the interior beads while still separately solving for the velocities of the end beads, we make use of the observations that the hydrodynamic drag typically changes sharply at the filament ends and changes slowly over the filament interior (see Sec. II B).

The rest of the paper is organized as follows. In Sec. II we show the theoretical development of the proposed approach organized in three parts. In part A we show the formulation of the implicit string-of-bead hydrodynamics. The hydrodynamic drag on each bead in a string-of-beads idealization is
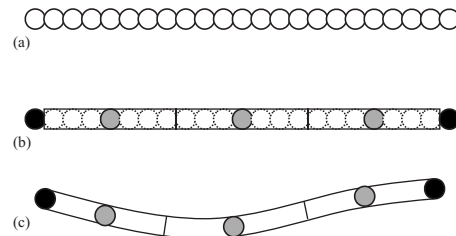

FIG. 1. Implicit and averaged hydrodynamics of semiflexible filaments. (a) In a string-of-beads realization of a semiflexible filament, the hydrodynamic drag on each bead can be determined by solving for the true relative velocity or hydrodynamic velocity of each bead. (b) Since the hydrodynamic velocity/drag is much larger at the end beads of a filament, and since the hydrodynamic velocities of the interior beads change slowly, sections of the interior beads (shown within rectangles) can be approximated by hydrodynamic velocities of representative beads within them (gray beads). Therefore instead of solving for the hydrodynamic velocities of the 23 beads in (a), we need to only solve for the hydrodynamic velocities of the two end beads and the three representative beads in (b). (c) The implicit hydrodynamic velocity technique is combined with an earlier string-of-rods idealization developed by the authors [6]. In it, the elastic response of a filament is calculated by considering each section of the filament as a cantilever beam, and by solving for the forces and bending degrees of freedom at the cantilever intersections. The drag force on each cantilever is determined from the hydrodynamic velocities of its representative bead and any associated end bead.

determined by implicitly solving for its relative or hydrodynamic velocity. In part B we show the formulation of the averaged implicit string-of-beads hydrodynamics. By assuming sections of interior beads to have a representative translational and rotational velocity, the implicit hydrodynamics is solved over fewer beads. In part C we show how the averaged implicit hydrodynamics method can be incorporated into an earlier model of a semiflexible filament in Brownian motion, which had assumed uniform friction coefficient along the filament [6]. An overall schematic of the proposed approach is shown in Fig. 1. In Sec. III we use the new model to simulate the Brownian fluctuation of a free and confined actin filament. We show that hydrodynamic interaction may have systematic effects on the Brownian conformations assumed by the filament, warranting detailed follow-up studies. We also show that hydrodynamic interaction with neighbors appears to confine a filament by increasing the filament's persistence length.

II. METHODS AND VALIDATION

A. Implicit string-of-beads hydrodynamics

The hydrodynamic drag on a bead is determined from its true relative velocity or hydrodynamic velocity, which is its observed velocity relative to the solvent flow at the bead center. The first-order Stokesian superposition approach obtains the solvent velocity at a bead as the summation of the solvent velocities due to each neighboring bead. The Method of Reflections improves on the first-order estimate by iteratively adding corrections so that the superposed solvent
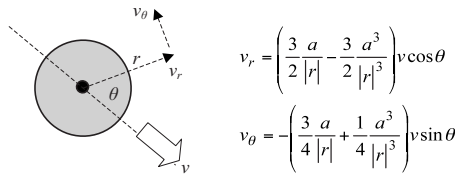
FIG. 2. Two-dimensional solvent field around a bead moving with velocity v in a fluid at rest. A bead moving in a dilute Stokesian solvent at rest induces a solvent flow around it. The induced solvent flow at any point can be determined as radial (v_r) and tangential (v_θ) velocities, which are functions of the radial separation r and angle from the flow θ. In this study, the cubic-order term in the solvent velocity equations is neglected.

flows are induced by the hydrodynamic velocities and not the observed velocities of the neighbors [10]. We use the same idea to improve on the first-order superposition estimate of the solvent field. However, instead of iteratively correcting for the hydrodynamic velocities as in the Method of Reflections, we solve for them implicitly. We illustrate this in more details below in the context of the hydrodynamic interaction between two beads moving alongside each other.

1. First-order linear superposition

Fig. 2 shows the two-dimensional solvent velocity field around a bead moving in a fluid at rest. The solvent field around the bead can be resolved into radial and tangential velocities, which can be determined at any point using the distance to the bead center and the angle relative to the bead velocity. Now consider two beads, I and II, moving with velocity v_1 and v_2 perpendicular to the line joining their centers [Fig. 3(a)]. A simple first-order superposition of their solvent velocity fields would *estimate* their relative velocities[1] (v_1^H and v_2^H) as,

$$v_1^H = v_1 - \frac{3a}{4|r_{12}|} v_2, \tag{1a}$$

$$v_2^H = v_2 - \frac{3a}{4|r_{12}|} v_1. \tag{1b}$$

However, if bead II were stationary ($v_2 = 0$), then by Eq. (1a), bead I would experience no hydrodynamic influence from it. The equation does not capture the hydrodynamic drag on bead I due to its solvent flow being reflected back by bead II. Alternatively if bead II were drifting in the solvent flow induced by bead I [$v_2 = v_1(\frac{3a}{4|r_{12}|})$], then by Eq. (1a), bead I would still experience a hydrodynamic influence from bead II, even though it is the solvent flow from its own motion that is causing bead II to move. Higher order superpositions of the solvent field would correct for these effects, and the Method of Reflections applies them iteratively [12,13].

[1]Throughout the paper we will assume that the overall solvent velocity is zero. We will use the term "relative velocity" to refer to the particle velocity relative to the local solvent velocity, and not relative to the overall solvent velocity.
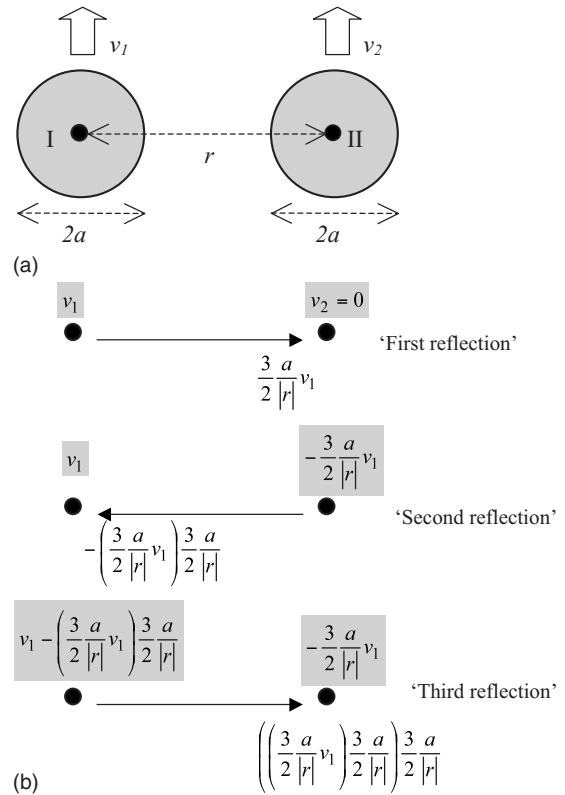

(a)

(b)

FIG. 3. Method of Reflections. (a) Consider the case of two beads, radius a and distance r apart, moving at velocities v_1 and v_2 perpendicular to the line joining their centers. Let A and B be the location of the centers of beads *I* and *II*. (b) Method of Reflections: For ease of description, consider $v_2 = 0$, and neglect the cubic-order term in the solvent velocity field of a bead (Fig. 2). The no-slip boundary condition requires that the solvent velocity and the bead velocity match at bead center. Due to the first-order superposition of the solvent field induced by bead I, the solvent velocity at bead II is no more zero. The Method of Reflections corrects for it by superposing a negative solvent field at B, so that the net velocity at Bead II is zero. Physically it means that the bead II is moving opposite to the local solvent flow around it, so that the observed velocity is zero. The corrective solvent field at bead II is now felt at bead I as $(3/2a/rv_1)3/2a/r$, leading to a mismatch again between the solvent and bead velocity at bead I. The Method of Reflections again corrects for the mismatch by adding on another solvent field at bead I. Physically the correction means that bead I is now moving relative to a local solvent velocity of $(3/2a/rv_1)3/2a/r$, instead of a local solvent at rest. Each solvent correction in the Method of Reflections can be seen as updating the relative/hydrodynamic velocity of a bead to ensure that solvent flow at it is induced by the recently updated hydrodynamic velocity of its neighbor.

2. Method of reflections

The Method of Reflections is an iterative technique that estimates the relative velocities and therefore hydrodynamic drag of particles in a Stokesian solvent, by explicitly adding higher-order corrections to the solvent field in each iteration [14]. Mathematically, each iteration serves to correct the solvent velocity field so that the no-slip boundary condition is enforced at the particle center [see Fig. 3(b) for more details]. Physically, this translates to iteratively correcting the

hydrodynamic influence on a particle to originate from the true relative velocity and not the observed velocity of its neighbors. For instance in the case of two beads moving alongside [Eqs. (1)], the next order correction in the Method of Reflections would be to the hydrodynamic velocity of bead I,

$$v_1^H = v_1 - \frac{3a}{4|r_{12}|}\left(v_2 - \frac{3a}{4|r_{12}|}v_1\right), \qquad (2a)$$

where the term within the brackets is but the first-order hydrodynamic/relative velocity of bead II [Eq. (1b)]. The correction is equivalent to saying that it is the relative velocity of bead II, and not its observed velocity, that causes the solvent flow at bead I. Similarly, the next order correction of the hydrodynamic velocity of bead II would appear as

$$v_2^H = v_2 - \frac{3a}{4|r_{12}|}\left[v_1 - \frac{3a}{4|r_{12}|}\left(v_2 - \frac{3a}{4|r_{12}|}v_1\right)\right], \qquad (2b)$$

where the term in the outer brackets is the previously updated hydrodynamic or relative velocity of bead I [Eq. (2a)]. To summarize, the iterative corrections of the Method of Reflections ensure that it is the updated hydrodynamic velocities that induce solvent flow and exert hydrodynamic effects. However, such an *explicit* iterative scheme becomes difficult to implement once the number of particles increases, even if only two reflections or correction orders are considered.

3. Implicit hydrodynamics

Instead of iteratively updating the hydrodynamic velocity with each reflection, the hydrodynamic velocity can be considered as a separate variable and solved for implicitly. For the case of two beads moving perpendicular to their center line [Fig. 3(a)], the implicit version of Eqs. (2) would be

$$v_1^H = v_1 - \frac{3a}{4|r_{12}|}v_2^H \qquad (3a)$$

$$v_2^H = v_2 - \frac{3a}{4|r_{12}|}v_1^H \qquad (3b)$$

By solving these two equations simultaneously, the hydrodynamic velocities, and therefore the hydrodynamic drags, of the two beads can be determined.

Figure 4 shows the predictions of the implicit technique for the change in the drag of a bead in the presence of another bead. Both beads are of the same radius, moving with the same velocity perpendicular and parallel to the line through their centers (see insets in Fig. 4). Note that the prefactor 3/4 in Eq. (3) changes to 3/2 for two beads moving parallel to their center line (see solvent field equations in Fig. 2). The drag correction is determined as the ratio of the bead's hydrodynamic velocity to its apparent relative velocity, v^H/v. The predictions of the implicit method show a better match to rigorous calculations [15,16] and experimental observations [17,18], than the predictions of a first-order superposition. The implicit technique predicts a smaller drag reduction than the first-order superposition technique. This is
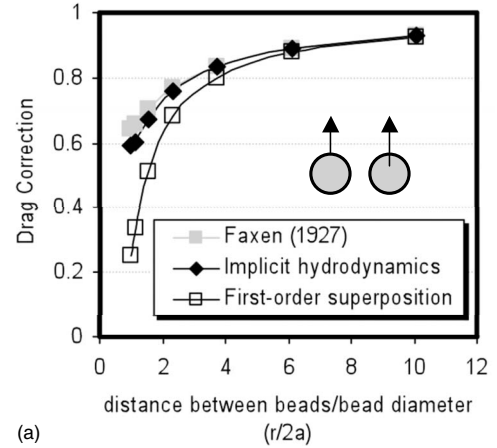
(a)
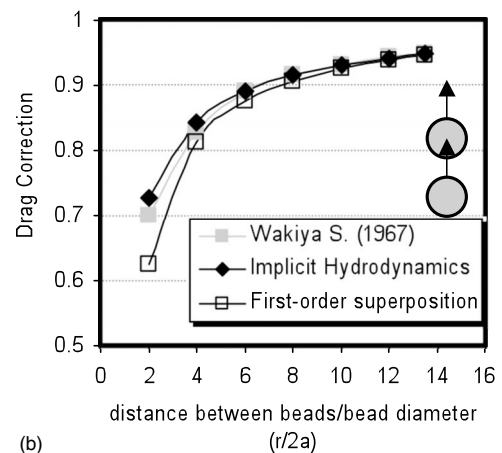
(b)

FIG. 4. The correction in the drag on a single bead from the presence of a neighboring bead moving at the same velocity, perpendicular (a) and parallel (b) to the center line. The plots show the drag correction predicted by the first-order superposition technique and by the implicit hydrodynamics technique. The predictions are compared against detailed calculations of the drag correction by Wakiya [15] and against experimental observations by Faxen [16].

because a component of a bead's velocity comes from drifting in the solvent flow induced by its neighbor. In the implicit technique, that component does not exert a drag-reducing hydrodynamic influence on the bead's neighbor. Finally, note that the solution of the first-order superposition is the same as that given by the first reflection in the Method of Reflections, and the solution of the implicit technique is the same as that given by infinite reflections in the Method of Reflections. The error between the implicit and the experimental/rigorous solutions in Fig. 4 is not because of Stokes superpositions, but comes from the approximations in the equations describing solvent flow around a bead (Fig. 2) [10].

4. Implicit hydrodynamics for a rigid rod in dilute solution

The hydrodynamic drag along a rigid rod can be estimated by idealizing it as a string of beads, and solving for the hydrodynamic velocities of the beads. We resolve the velocities of a rigid rod and a bead in the following way. The

two-dimensional motion of a rigid rod can be described completely by three velocities: the translational velocity of the rod center in the direction normal to the rod (V^n), the translational velocity of the rod center in the direction parallel to the rod (V^p), and the rotational velocity about the rod center (W). The motion of any bead within the rod can be described completely by two velocities: the translational velocity normal to the rod (v^n), and the translational velocity parallel to the rod (v^p). We use upper-case letters to denote rod velocities, and lower-case letters to denote bead velocities. The relation between the velocities of the ith bead and that of the rigid rod are,

$$v_i^n = V^n + Wr_{ic},$$ (4a)

$$v_i^p = V^p,$$ (4b)

where r_{ic} is the distance of the ith bead from the rod center c.

The true relative velocity or the hydrodynamic velocity of the ith bead can be determined by extending Eq. (3) to include the hydrodynamic influence from the rest of the beads within the rod. Using appropriate prefactors for the hydrodynamic influence,

$$\begin{pmatrix} v_i^{pH} \\ v_i^{nH} \end{pmatrix} = \begin{pmatrix} V^p \\ V^n + r_{ic}W \end{pmatrix} - \sum_{j=1, j \neq i}^{M} \begin{pmatrix} \dfrac{3a_j}{2|r_{ij}|} \\ \dfrac{3a_j}{4|r_{ij}|} \end{pmatrix} \bullet \begin{pmatrix} v_j^{pH} \\ v_j^{nH} \end{pmatrix}.$$ (5)

Here M is the number of beads composing the rod, and v_i^{pH} and v_i^{nH} are the hydrodynamic velocities of the ith bead, parallel and normal to the rod.

The total drag force experienced by a rigid string of M beads is known to be much smaller than the total drag force experienced by M separate beads. This is due to hydrodynamic screening—the solvent flow set up by the motion of one bead reduces the relative velocity and therefore drag experienced by a neighboring bead. Figures 5(a) and 5(b) show the hydrodynamic velocity profile of the beads along a rigid rod in pure normal and rotational motion, scaled respectively by the normal and rotational velocity of the rod. The profile was determined by solving Eq. (5) simultaneously for all beads within the rod (for $i=1$ to M). The profiles are shown for rod sizes of 20, 60, and 100 beads. For a rigid rod in pure normal translation, the normal velocity of each bead is uniform along the rod; but the normal hydrodynamic velocity [Fig. 5(a)] is higher at the rod's ends and decreases toward the interior, giving a "U" shape. For a rigid rod in pure rotation, the normal velocity of each bead increases linearly in opposite directions away from the rod center. The normal hydrodynamic velocity [Fig. 5(b)], however, increases faster at the rod ends than in the rod interior. The highest hydrodynamic velocities, and therefore drag, occur on the bead at each rod end. We refer to them as "end beads," and refer to the rest of the beads as "interior beads." The hydrodynamic velocities in the interior beads decrease toward the center of the rod. It appears that the beads in the central region of the rod are nearly drifting in the solvent flow setup by the motion of their neighbors on either side, and therefore experience a decreased relative velocity and
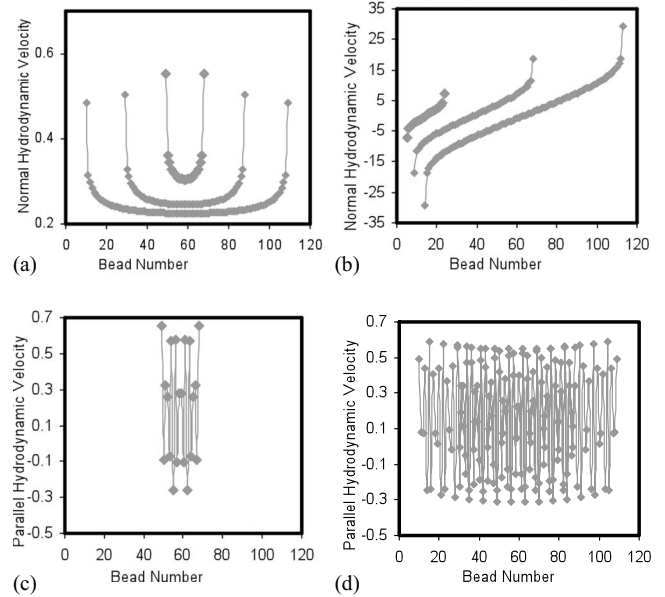

FIG. 5. Profile of bead hydrodynamic velocities along a rigid rod in normal, rotational, and parallel motion. (a) The normal hydrodynamic velocity profile of beads constituting a rigid rod in pure normal translation. The hydrodynamic velocities are scaled by the normal velocity of the rod. Three rod sizes of 20, 60, and 100 beads are shown, with the profiles displaced by 50, 30, and 10 beads, respectively. (b) The normal hydrodynamic velocity profile of beads constituting a rigid rod in pure rotation. The hydrodynamic velocities are scaled by the rotational velocity of the rod. Three rod sizes of 20, 60, and 100 beads are shown, with the profiles displaced by 5, 10, and 15 beads, respectively. (c,d) The parallel hydrodynamic velocity profile of beads constituting a rigid rod in parallel translation. The hydrodynamic velocities are scaled by the parallel velocity of the rod. Rod sizes of 20 [Fig. 5(c)] and 100 [Fig. 5(d)] beads are shown, with the profiles displaced by 50 and 10 beads, respectively.

drag. The end beads, on the other hand, do not experience the full benefit of hydrodynamic screening and have larger hydrodynamic velocities.

For a rigid rod in pure parallel and tangential motion, the parallel velocity of each bead is uniform along the rod. In Figs. 5(c) and 5(d), we show the parallel hydrodynamic velocities of the beads, for rods of 20 and 100 bead sizes. The hydrodynamic velocities are scaled by the parallel velocity of the rod. The profile shows large bead-to-bead fluctuations in hydrodynamic velocities, with no definite overall trend. We found these fluctuations to be mathematical artifacts. They disappear upon inclusion of the cubic term in the Stokes solution for the solvent field around a bead (Fig. 2), and the profile takes on a U shape similar to that of the normal hydrodynamic velocities in Fig. 5(a) (data not shown). However, we omit the cubic-order term and the attendant increase in mathematical complexity because (1) the omission of the cubic-order term leads the less than 5% error in the total drag calculations for a rigid filament, and (2) the fluctuations disappear when the hydrodynamic velocities are determined as section averages (see Sec. II B).

In Fig. 6 we show validations of the filament hydrodynamic profile obtained with the implicit method. First, the
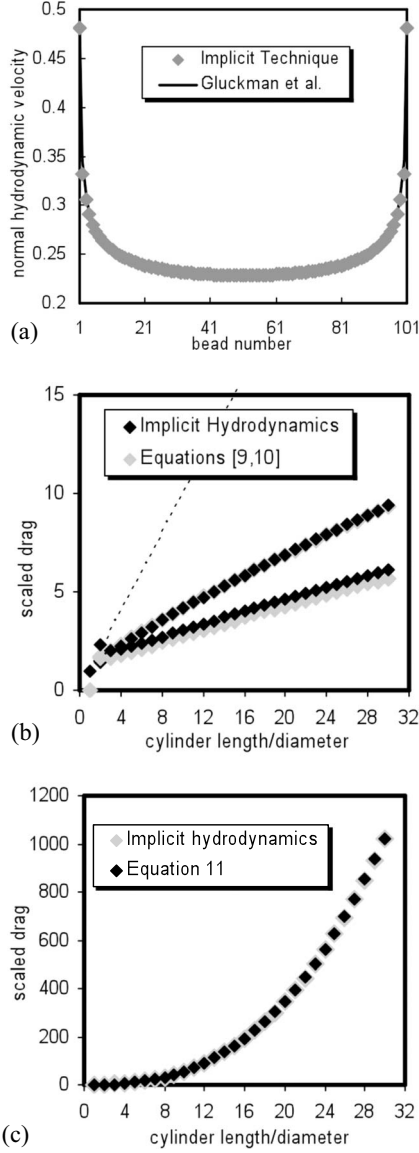
(a)

(b)

(c)

FIG. 6. Validation of the implicit hydrodynamic technique. (a) The scaled frictional drag or hydrodynamic velocity profile along a rigid rod of 101 beads in normal translation, compared against the predictions of Gluckman *et al.* [14]. (b) The total frictional drag on rigid rods of different lengths in normal and parallel motion, compared against standardized equations. The vertical axis shows the total frictional drag of the rod scaled by that of a single bead. The horizontal axis shows the number of beads constituting the rod. In the absence of hydrodynamic screening between the beads of the rod, the translational frictional drag would fall along the dashed line of slope 1. (c) The scaled frictional drag on rigid rods of different lengths in rotational motion, compared against standardized equations.

increased drag at the ends for a rigid rod in normal translation is in agreement with the observations of Lagamarsino *et al.* [7]. Figure 6(a) shows that the normal hydrodynamic velocity profile for a string of 101 beads compares well against that determined by Gluckman *et al.* [14] using detailed calculations. In Figs. 6(b) and 6(c), we show the total friction drag predicted for a rigid rod in translation and rotation, by the implicit method and by standard equations [Eqs.

(6a)–(6d)]. The friction drag is scaled by the velocity of the rigid rod. In the implicit method, the total friction drag is calculated as $\Sigma_{i=1}^{M} \frac{v_i^{jH}}{V^j}$ with $j=n,p,r$ for rods in normal, parallel and rotational motion. The predictions of the implicit method compare well against standard expressions for ξ^j / ξ^{sph} [Eqs. (6a)–(6d)], where ξ^j is the parallel, normal and rotational friction coefficient of a rigid cylinder (for $j=p,n,r$, respectively), and ξ^{sph} is the friction coefficient of a sphere.

$$\xi^p = \frac{8\pi\eta L}{\ln\left[\dfrac{L}{d} + \lambda^p\right]}, \tag{6a}$$

$$\xi^n = \frac{4\pi\eta L}{\ln\left[\dfrac{L}{d} + \lambda^n\right]}, \tag{6b}$$

$$\xi^r = \frac{\pi\eta L^3}{3\ln\left[\dfrac{L}{d} + \lambda^r\right]}, \tag{6c}$$

$$\text{and} \quad \xi^{sph} = 6\pi\eta a, \tag{6d}$$

where K, T, and η are the Boltzmann constant, temperature and solvent viscosity, respectively. λ^p, λ^n, and λ^r are correction terms added to the frictional coefficient equations to include the effects of the cylinder ends on the cylinder diffusion. The correction terms are equal to -0.114, 0.886, and -0.447, respectively [19,20]. It is interesting to note that the implicit technique intrinsically accounts for these end corrections.

5. Generalized equations for implicit hydrodynamics

In Sec. II A 2 we described the implicit method for two beads moving parallel and perpendicular to their center line. The equations in Sec. II A 2 can be easily extended to capture the hydrodynamic influence between beads moving at arbitrary velocities and directions. We demonstrate for the case of two beads which are parts of two different rods separated by an arbitrary angle and distance (Fig. 7).

Let beads I and II be part of two separate rods. Let V_1^p, V_2^p and V_1^n, V_2^n be the parallel and normal translational velocities of the rods, and let θ_1, θ_2 be their orientation angles (Fig. 7). Let v_1^p, v_2^p and v_1^n, v_2^n be the corresponding parallel and normal velocities of the beads of interest, and let θ_{12} and r_{12} be the angle and distance between them (Fig. 7). The *hydrodynamic influence of bead II on bead I* can be determined as

$$\begin{pmatrix} v_1^{pH} \\ v_1^{nH} \end{pmatrix} = \begin{pmatrix} V_1^p \\ V_1^n \end{pmatrix} - H_{12} \begin{pmatrix} v_2^{pH} \\ v_2^{nH} \end{pmatrix}, \tag{7}$$
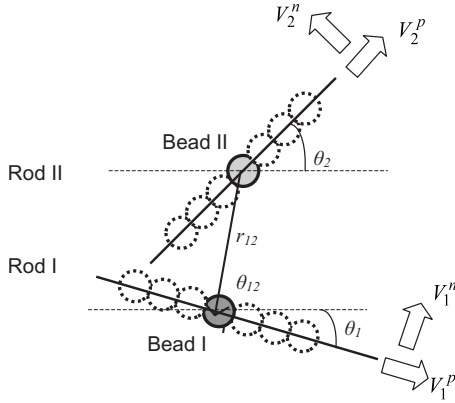
where

FIG. 7. Generalized hydrodynamic influence of bead II on bead I.

$$H_{12} = \begin{pmatrix} \cos(\theta_{12} - \theta_1) & -\sin(\theta_{12} - \theta_1) \\ \sin(\theta_{12} - \theta_1) & \cos(\theta_{12} - \theta_1) \end{pmatrix}$$
$$\times \begin{pmatrix} \dfrac{3a}{2|r_{12}|}\cos\theta_{12} & \dfrac{3a}{2|r_{12}|}\sin\theta_{12} \\ -\dfrac{3a}{4|r_{12}|}\sin\theta_{12} & \dfrac{3a}{4|r_{12}|}\cos\theta_{12} \end{pmatrix} \quad (8)$$

H_{12} is a matrix describing the hydrodynamic influence of bead II on bead I. It has two component matrices [Eq. (8)]. The right-side matrix determines the radial and tangential solvent field due to bead II at the location of bead I. Multiplication by the left-side matrix projects the radial and tangential solvent velocities at bead I in the directions of its parallel and normal velocities. Following trigonometric simplification, H_{12} can be reduced to

$$H_{12} = \frac{3}{4}\frac{a}{|r_{12}|}\begin{pmatrix} \cos\theta_1 & \sin\theta_1 \\ -\sin\theta_1 & \cos\theta_1 \end{pmatrix}$$
$$\times \begin{pmatrix} 1 + \cos^2\theta_{12} & \cos\theta_{12}\sin\theta_{12} \\ \cos\theta_{12}\sin\theta_{12} & 1 + \sin^2\theta_{12} \end{pmatrix}. \quad (9)$$

The right-side matrix gives the solvent velocity that is induced by bead II at bead I, projected along the *x* and *y* directions. The left-side matrix projects that solvent velocity into directions parallel and normal to bead I.

Figure 8 illustrates the use of Eqs. (7) and (9) to determine the change in the hydrodynamic velocity profile of a rigid rod in normal translation (rod I), from the presence of neighboring rigid rod which is stationary (rod II). The plots are determined for three different angles and distances between the rods [Fig. 8(d)]. The normal translation of rod I is opposed by the presence of the stationary rod II, and correspondingly the normal hydrodynamic velocities (and therefore drag) increases in regions close to rod II [Fig. 8(a)–8(c)]. For instance, the bead hydrodynamic velocities of rod I increase in the region away from its center, due to a parallel neighboring rod located there; and the increase is greater toward the rod end [Fig. 8(a), and case (a) in Fig. 8(d)]. When the neighboring rod is located perpendicular toward the center of rod I, the normal hydrodynamic velocities
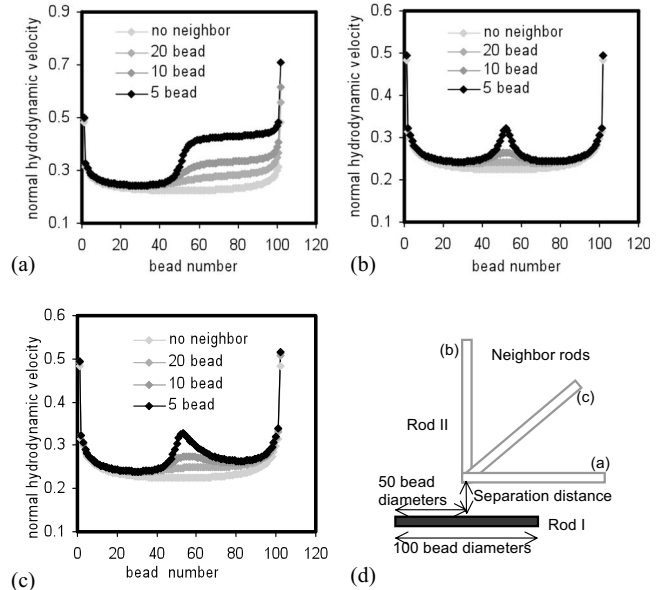

FIG. 8. The change in the normal hydrodynamic velocity profile of a rigid rod in normal translation from presence of a neighboring stationary rod. Panels (a), (b), and (c) show the change in the normal hydrodynamic velocities of rod I, for three angles of the stationary neighboring rod II: 0°, 45°, and 90°, respectively. Panel (d) shows the relative positions of the two rods for the three cases. Rod I is shown as a black filled rod, and rod II is shown as a gray, unfilled rod. The distances of separation between the rods are 5, 10, 20 and infinite bead diameters.

increase locally there [Fig. 8(b), and Fig. 8(d) case (b)]. As expected, the hydrodynamic velocity profile due to a neighboring rod that is positioned at an angle, appears to be some combination of the profiles due to a parallel and perpendicular neighbor [Fig. 8(c), and Fig. 8(d) case (c)]. It is interesting that the increase in hydrodynamic velocities occurs only in regions adjacent to the neighbor, and the increase becomes negligible by 50 bead diameters of separation (not shown).

We also compared the sedimentation velocity of a tetramer (4 beads at the corner of a square, and touching each other) that is predicted by the implicit technique, against that measured experimentally in Swanson *et al.* [21]. The implicit hydrodynamics technique experimental method gave a sedimentation velocity of 0.4447 ± 0.0004 relative to that of a free bead [21].

B. Averaged implicit hydrodynamics

While the implicit method is relatively straightforward and captures the end effects and hydrodynamic screening that govern the diffusion of rigid rods, it is computationally expensive. The technique introduces at least two new hydrodynamic variables per bead, and the computational cost of an implicit matrix solution scales as N^2, where N is the total number of variables.

1. Averaged implicit hydrodynamics for a rigid rod

The normal and parallel hydrodynamic velocity profiles along a rigid rod in pure translation or rotation [Figs. 5(a)

and 5(b)] suggests that sections of the interior beads can be approximated by a single normal, parallel and rotational hydrodynamic velocity. *That is, the normal and parallel hydrodynamic velocity profile over a section of the interior beads can be approximated from the normal, parallel and rotational hydrodynamic velocity of the central bead, c, in the section.* For the ith bead in a section, the approximated normal and parallel hydrodynamic velocities are

$$v_i^{nH} = v_c^{nH} + w_c^H r_{ic}, \tag{10a}$$

$$v_i^{pH} = v_c^{pH}. \tag{10b}$$

We refer to the central bead in a section as the *representative* bead of that section. The parallel hydrodynamic velocity profile of the interior beads fluctuate over a small length scale with no definite trend (Fig. 5(c) and 5(d)). Therefore no useful information is lost when fluctuating velocities are replaced by a constant value. In all, by assuming each section of interior beads to have constant hydrodynamic velocities, the implicit hydrodynamic equations need to be written and solved for only one representative bead per section, and for each end bead. This considerably reduces the cost of the implicit solution. Also, by not considering the end beads as part of a section, the large localized drag on them is still captured, and the hydrodynamic profile over the rod is more effectively approximated.

The angular hydrodynamic velocity of a representative bead cannot be solved in a form similar to the normal hydrodynamic equation. It will result in a trivially zero equation if a representative bead were located in the center of the rod ($r_{cc} = 0$). Instead, we determine the hydrodynamic angular velocity about the representative bead as *the differential of its normal hydrodynamic velocity profile there.* That is, we determine it as the change in normal hydrodynamic velocity experienced by the bead, if it translated an infinitesimal distance along the rod. If c be the representative central bead of a section,

$$w_c^H = \frac{1}{2a} \frac{d}{di} (v_i^{nH})|_c. \tag{11}$$

For simplicity, we first demonstrate the averaging technique by grouping the interior beads of a rigid rod into a *single*

section. The hydrodynamic equation for the normal, parallel and rotational hydrodynamic velocities about bead c can be written using Eqs. (5) and (11), and grouping beads with the same hydrodynamic velocities,

$$\begin{pmatrix} v_c^{pH} \\ v_c^{nH} \\ w_c^H \end{pmatrix} \cdot \underbrace{\begin{pmatrix} 1 + \sum_{j=2, j \neq c}^{M-1} \frac{3a}{2|r_{cj}|} \\ 1 + \sum_{j=2, j \neq c}^{M-1} \frac{3a}{4|r_{cj}|} \\ 1 + \sum_{j=2, j \neq c}^{M-1} \left(\frac{3a}{4|r_{cj}|} \right) \end{pmatrix}}_{\substack{\text{Hydrodynamic influence of section} \\ \text{on its representative bead}}}$$

$$= \begin{pmatrix} V^p \\ V^n \\ W \end{pmatrix} - \sum_{j=1,M} \underbrace{\begin{pmatrix} \frac{3a}{2|r_{cj}|} & 0 & 0 \\ 0 & \frac{3a}{4|r_{cj}|} & 0 \\ 0 & \frac{3a}{4|r_{cj}|^2} & 0 \end{pmatrix}}_{\substack{\text{Hydrodynamic influence of end bead} \\ \text{on representative bead of section}}} \cdot \begin{pmatrix} v_j^{pH} \\ v_j^{nH} \\ 0 \end{pmatrix} \tag{12}$$

The summation in the left hand side of Eq. (12) is over all interior beads comprising the section. The summation in the right hand side of the equation [Eq. (12)] is over the end beads, $j = 1, M$. The first matrix gives the hydrodynamic influence on bead c from within its section, and the second matrix gives the hydrodynamic influence on bead c from the end beads. We use the symbols H_S and H_{SE} to refer to the two matrices, respectively.

Similarly the hydrodynamic equations for each end bead can be written in the single-section averaging scheme. Note that the angular hydrodynamic velocity equation is not required for the end beads. Writing Eq. (5) for $i = 1, M$ and grouping the interior beads with the same hydrodynamic velocities,

$$\begin{pmatrix} v_i^{pH} \\ v_i^{nH} \end{pmatrix} = \begin{pmatrix} V^p \\ V^n + W r_{ic} \end{pmatrix} - \underbrace{\begin{pmatrix} \sum_{j=2}^{M-1} \frac{3a}{2|r_{ij}|} & 0 & 0 \\ 0 & \sum_{j=2,}^{M-1} \frac{3a}{4|r_{ij}|} & \sum_{j=2}^{M-1} r_{jc} \frac{3a}{4|r_{ij}|} \end{pmatrix}}_{\text{Hydrodynamic influence of section on end bead } (H_{ES})} \begin{pmatrix} v_c^{pH} \\ v_c^{nH} \\ w_c^H \end{pmatrix} - \underbrace{\begin{pmatrix} \frac{3a}{2|r_{ik}|} & 0 \\ 0 & \frac{3a}{4|r_{ik}|} \end{pmatrix}}_{\substack{\text{Hydrodynamic influence of end} \\ \text{bead on end bead } (H_{EE})}} \times \begin{pmatrix} v_k^{pH} \\ v_k^{nH} \end{pmatrix}_{\substack{k=1,M \\ k \neq i}} \tag{13}$$
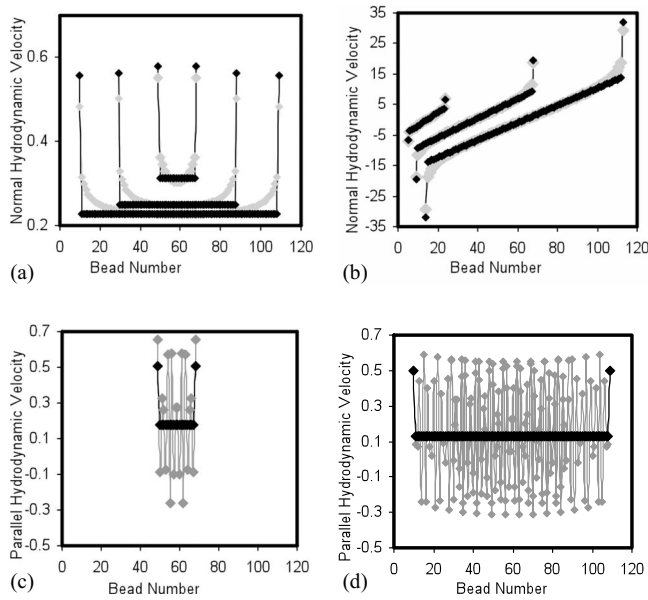
FIG. 9. Approximation of the bead hydrodynamic velocity profile of Fig. 5 by assuming all interior beads to have uniform normal, parallel, and rotational hydrodynamic velocities (that of the representative beads). The bead hydrodynamic velocity profiles are shown in gray and their approximations are shown in black.

The summation in the first matrix is over all interior beads comprising the section of beads. The first matrix gives the hydrodynamic influence of the section on the end bead (H_{ES}), and the second matrix gives the hydrodynamic influence of one end bead on another (H_{EE}).

To summarize, the averaging procedure therefore consists of two ideas. The first idea is that the normal and parallel hydrodynamic velocity profiles over sections of interior beads can be approximated by the normal, parallel and rotational hydrodynamic velocity of the central bead in that section. The second is that the angular hydrodynamic velocity about the representative bead can be determined by the differential of the normal hydrodynamic velocity profile there. It is important to note that in this averaging technique, the hydrodynamic equation written for a bead still includes the hydrodynamic influences of all its neighboring beads. However, the number of beads for which the hydrodynamic equations need to be solved is reduced, thereby decreasing the computational cost.

In Figs. 9(a)–9(d) we show the single-section averaging of the hydrodynamic velocity profiles of Figs. 5(a)–5(d). The interior beads have uniform normal, rotational and parallel hydrodynamic velocities for the respective cases of a rod in pure normal, rotational, and parallel motion; and the end beads show much higher hydrodynamic velocities. The total drag calculated by summing the averaged profile matches that predicted by standard equations and by the implicit string-of-beads method [see Figs. 6(b) and 6(c)].

2. Averaged implicit hydrodynamics for multiple sections and rigid rods

The above averaging technique can be extended to the interaction between multiple sections within a rod, to the
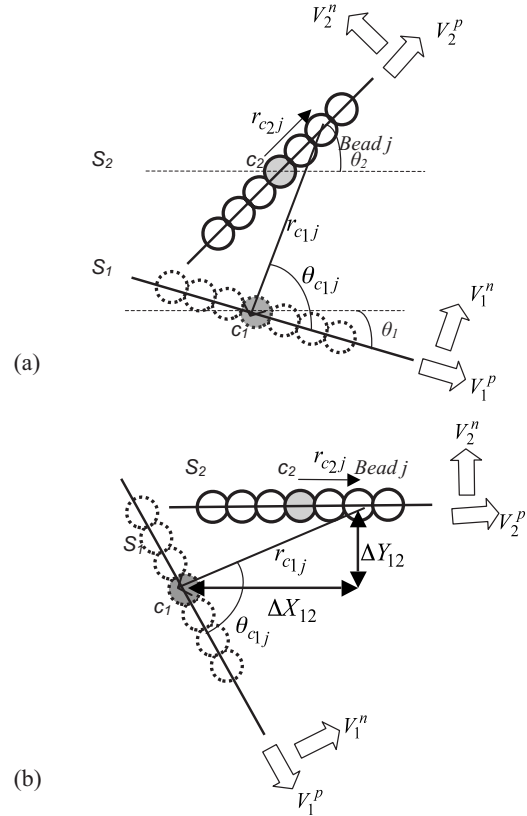

FIG. 10. Capturing the hydrodynamic influence of the beads of section S_2 on the representative bead of section S_1. (a) The distance r_{jc_1} and the angle θ_{jc_1} between c_1 and bead j of section S_2, vary for each bead when integrating through the beads of S_2. (b) A simple rotation of frame so that section S_2 lies along the horizontal axis, makes r_{jc_1} and θ_{jc_1} a function of only one variable x_{jc_1}.

interaction between multiple rods. The hydrodynamic equations now require generalized expressions for the hydrodynamic influence of one end bead or section of beads on the representative bead of a section or on an end bead. The hydrodynamic influence of an end bead on another end bead or representative bead can be determined using Eq. (9) of Sec. II A 4. The equation describes the hydrodynamic influence of one arbitrarily placed bead on another. Here we describe the calculation of the hydrodynamic influence of one section of beads on the representative bead of another section. The hydrodynamic influence of a section on an end bead is similarly calculated, except that the self interaction matrix H_S is unity for an end bead [the summation terms in H_S of Eq. (12) do not exist for an end bead].

Consider two sections, $S1$ and $S2$, which are parts of two separate rigid rods (Fig. 10). Let V_1^p, V_2^p and V_1^n, V_2^n be the parallel and normal translational velocities of the sections; θ_1 and θ_2 be their orientation angles; and c_1 and c_2 be their representative central beads. Let θ_{c_1j} and r_{c_1j} be the angle and distance between c_1 and the jth bead of section $S2$ (Fig. 10). Let sections $S1$ and $S2$ be composed of M interior beads. Using the previously described notation for the hydrodynamic velocities, the equation for the hydrodynamic

influence of sections $S1$ and $S2$ on the representative bead of section $S1$ is given as

$$
\begin{bmatrix} v_{c_1}^{pH} \\ v_{c_1}^{nH} \\ w_{c_1}^{H} \end{bmatrix} \cdot H_{S_1} = \begin{bmatrix} V_1^p \\ V_1^n \\ W_1 \end{bmatrix} - H_{S_1 S_2} \begin{bmatrix} v_{c_2}^{pH} \\ v_{c_2}^{nH} \\ w_{c_2}^{H} \end{bmatrix}, \tag{14}
$$

where

$$
H_{S_1} = \frac{3}{4} a \begin{pmatrix} 1 + \sum\limits_{j=1, j \neq c}^{M} \dfrac{3a}{2|r_{c_1 j}|} \\ 1 + \sum\limits_{j=1, j \neq c}^{M} \dfrac{3a}{4|r_{c_1 j}|} \\ 1 + \sum\limits_{j=1, j \neq c}^{M} \dfrac{3a}{4|r_{c_1 j}|} \end{pmatrix}_{j \in S_1}, \tag{15}
$$

$$
H_{S_1 S_2} = \begin{pmatrix} \cos \theta_1 & \sin \theta_1 & \sin \theta_1 \\ -\sin \theta_1 & \cos \theta_1 & \cos \theta_1 \\ -\sin \theta_1 & \cos \theta_1 & \cos \theta_1 \end{pmatrix}
$$

$$
\times \begin{pmatrix} -\int_{j=1}^{M} \left(\dfrac{1 + \cos^2 \theta_{c_1 j}}{r_{c_1 j}} \right) dj & -\int_{j=1}^{M} \left(\dfrac{\sin \theta_{c_1 j} \cos \theta_{c_1 j}}{r_{c_1 j}} \right) dj & -\int_{j=1}^{M} r_{c_2 j} \left(\dfrac{\sin \theta_{c_1 j} \cos \theta_{c_1 j}}{r_{1 j}} \right) dj \\ -\int_{j=1}^{M} \left(\dfrac{\sin \theta_{c_1 j} \cos \theta_{c_1 j}}{r_{c_1 j}} \right) dj & -\int_{j=1}^{M} \left(\dfrac{1 + \sin^2 \theta_{c_1 j}}{r_{c_1 j}} \right) dj & -\int_{j=1}^{M} r_{c_2 j} \left(\dfrac{1 + \sin^2 \theta_{c_1 j}}{r_{c_1 j}} \right) dj \\ \dfrac{d}{ds} \int_{j=1}^{M} \left(\dfrac{\sin \theta_{c_1 j} \cos \theta_{c_1 j}}{r_{c_1 j}} \right) dj & \dfrac{d}{ds} \int_{j=1}^{M} \left(\dfrac{1 + \sin^2 \theta_{c_1 j}}{r_{c_1 j}} \right) dj & \dfrac{d}{ds} \int_{j=1}^{M} r_{c_2 j} \left(\dfrac{1 + \sin^2 \theta_{c_1 j}}{r_{c_1 j}} \right) dj \end{pmatrix}_{j \in S_2}, \tag{16}
$$

$$
\text{where} \quad \frac{d}{ds} = \frac{1}{2a} \frac{d}{di} \bigg|_c. \tag{17}
$$

H_{S1} is the matrix showing the hydrodynamic influence of $S1$ on its central representative bead c_1, and is similar to H_S in Eq. (12). H_{S1S2} is the matrix showing the hydrodynamic influence of the beads of $S2$ on the representative bead c_1. It is derived from the matrix describing the generalized hydrodynamic influence of one bead on another [Eq. (9)], but is integrated over all beads of section $S2$ to capture the hydrodynamic influence of section $S2$ on c_1. Also, H_{S1S2} includes the hydrodynamic influence of section $S2$ on the averaged angular hydrodynamic velocity of S1—obtained as the differential change in the normal hydrodynamic velocity profile along $S1$ at c_1, induced by the presence of section $S2$.

The integrals in H_{S1S2} are difficult to evaluate as both r_{c1j} and θ_{c1j} vary from bead to bead along section $S2$. Instead, we evaluate them by rotating the frame so that $S2$ now lies along the horizontal axis [Fig. 9(b)]. This makes r_{c1j}, $\sin \theta_{c1j}$ and $\cos \theta_{c1j}$ within the integral a function of only one variable, x_{c2j} and the constants ΔX_{12} and ΔY_{12},

$$
r_{c1j}^2 = [\Delta X_{12} - x_j]^2 + \Delta Y_{12}^2, \tag{18a}
$$

$$
\cos \theta_{c_1 j} = \frac{\lfloor \Delta X_{12} - x_j \rfloor}{r_{c_1 j}}, \tag{18b}
$$

$$
\sin \theta_{c_1 j} = \frac{\Delta Y_{12}}{r_{c_1 j}}, \tag{18c}
$$

where x_{c2j} is the distance between the jth bead of section S_2 and its central bead c_2. ΔX_{12} and ΔY_{12} are the horizontal and vertical distance between the central beads in the new reference frame. It is noted that the subscript j indicates a bead belonging to section S_2 in the above three equations.

Fig. 11 shows the averaged hydrodynamic profile of the 100 bead rod in Fig. 8 for the case of a 10 bead separation from its neighbor. The rods were averaged using 10 and 20 sections per rod. As shown in Fig. 11, the averaging technique reproduced the profile of the bead hydrodynamic velocities to a good degree, with the fit improving with increasing sections per rod.

C. Incorporating implicit hydrodynamics in Brownian dynamics of semiflexible filaments

We now demonstrate how the implicit bead hydrodynamics can be incorporated into a string-of-beads idealization of a *semiflexible* filament, and then show how the averaged implicit hydrodynamics can be included in a *string-of-rods idealization* of a semiflexible filament that was earlier developed by the authors [6].

1. String-of-beads idealization of semiflexible filament

In a string-of-beads representation, the Brownian dynamics of a semiflexible filament is usually determined by solving the particle form of the Langevin dynamics equation over each bead. The Langevin dynamics equations govern the balance between its frictional drag force, conservative force (F^P), and random Brownian forces (F^B). At each bead i,

$$\xi v_i(t) = F_i^P(t) - F_i^B(t), \tag{19}$$

where ξ is the frictional coefficient of a bead, and v is the bead velocity. Typical conservative forces (F^P) are bending and stretching forces which depend on the relative positions of the beads. The Brownian force (F^B) at each bead is obtained from a Gaussian distribution whose variance is given by the fluctuation dissipation theorem as

$$\langle F^B(t)F^B(t')\rangle = 4KT\xi\delta(t-t'). \tag{20}$$

In this Langevin dynamics setting, we incorporate hydrodynamic interaction by having the *frictional drag* on a bead be determined by its *hydrodynamic* or true relative velocity (v^H) rather than its observed velocity v.

$$\xi v_i^H(t) = F_i^P(t) - F_i^B(t). \tag{21}$$

Solving Eqs. (21) and (7) (equation for the bead hydrodynamic velocity) for all beads simultaneously, the Brownian dynamics of the semiflexible filament can be determined with the hydrodynamics included.

2. String-of-rods idealization of semiflexible filament

As discussed previously, solving for the hydrodynamics implicitly in a string-of-beads idealization introduces at least two new variables per bead, increasing the size of the computational problem. Instead, we can use the idea of grouping interior beads in sections and solving for the hydrodynamic velocities of the representative bead alone (see Sec. II B 2) in a string-of-rods idealization of a semiflexible filament [6] [Fig. 1(d)]. We briefly describe the string-of-rods idealization below, and then show how the averaged implicit hydrodynamics can be easily included in it.

In a string-of-rods idealization, a semiflexible filament is treated like a string of contiguously bending rods or segments [Fig. 12(a)], and the Brownian dynamics determined by solving equations at the segment intersections. The main ideas of the formulation are [6]:

(i) The semiflexible filament is divided into *segments* [Fig. 12(a)]. At each segment intersection or node the following six variables are solved for: the x and y displacements of the intersection, the filament angle θ and the curvature $d\theta/ds$ at the intersection, and the x and y forces arising at the cut face of the intersection. From the x and y forces, the differential of the filament curvature, $d^2\theta/ds^2$, at the intersection can be determined.

(ii) The dynamics of a segment is determined by the balance of three forces acting on it: the Brownian and drag forces acting along its length, and the forces arising at the cut face of its ends [6].

(iii) The Brownian forces distributed along the curved segment are resolved in the following way: the normal/
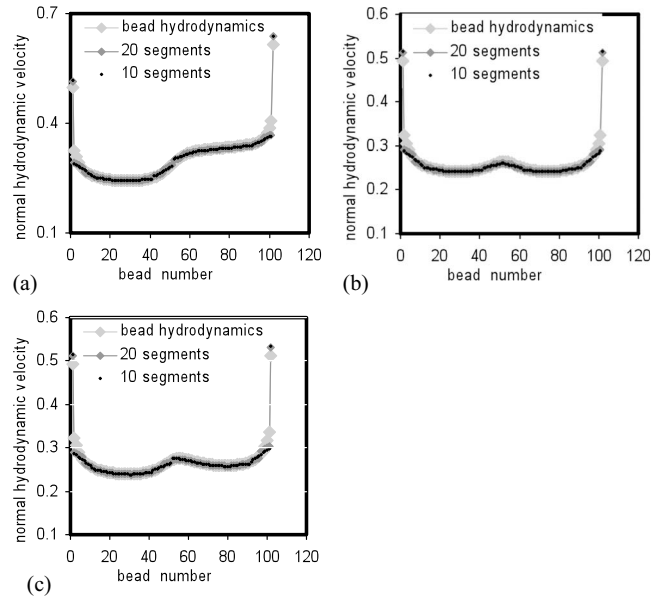

FIG. 11. Averaged hydrodynamic profile of the 100-bead rod in Figs. 8(a)–8(c) shown only for the case of a 10 bead separation from its neighbor. The rods were averaged using 10 and 20 sections.

parallel Brownian forces along the segment can be projected in two mutually perpendicular directions (u_1- and u_2-), and the projections can then be resolved into normal/parallel resultant forces and couples acting at the center of each projection [Fig. 12(b)]. The variance of the resultant forces and couples can be shown determined by the friction coefficients of rigid cylindrical rods [Eqs. (6)].

(iv) The drag forces distributed along the segment length are similarly resolved. The normal/parallel drag forces along a curved segment is projected in two mutually perpendicular directions (u_1- and u_2-), and the projections can then be re-
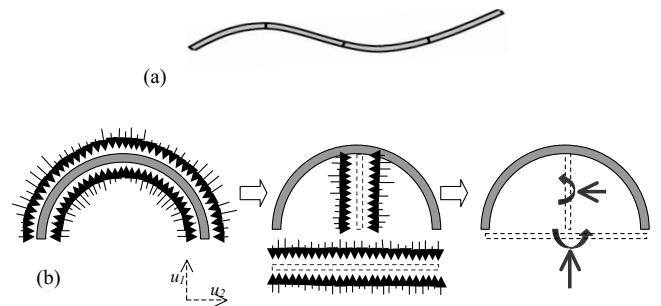

FIG. 12. Rods-on-string idealization of semiflexible filaments. (a) The rods-on-string idealization treats a semiflexible filament as a string of continuously bending rods or segments. The filament variables at the rod intersections or nodes are solved for. (b) The forces on a curved segment are resolved into their projections in two mutually perpendicular directions. The mutually perpendicular directions are taken to be along the line joining the segment ends (u_1), and along the line perpendicular to it (u_2). The projected forces in each direction are further resolved into a resultant force and couple in that direction. Solving for the force and moment balance equations over an instantaneously rigid rod requires only knowing the resultant forces and couples. In panel (b) only the distributed forces normal to the curved segment are considered.

solved into a normal/parallel resultant forces and couples acting at the center of each projection. The normal/parallel drag forces along the segment are calculated from the displacements along the segment, normal and parallel to it.

(v) For such a force resolution, the force and moment balance equations in the large-strain Euler bending theory can be used to solve for the filament curvature, $d\theta/ds$, and the x and y forces at the segment intersections. Also, the integral of the Euler moment-balance equation can be used to solve for the filament angle, θ, at the segment intersections.

(vi) For each segment, θ, $d\theta/ds$, and $d^2\theta/ds^2$ at its two ends are known. Therefore, using a fifth-order polynomial interpolation, $\theta(s)$ can be determined as a function the segment's contour, s. Then by integrating the sine and cosine projections of $\theta(s)$, the x- and y-length projections of the segment can be determined. From the change in the x- and y-length projections at each time-step, the x and y displacements of the segment intersections are solved for.

(vii) At each time-step, the six equations are assembled for each segment and the entire equation set for the filament is solved simultaneously.

(viii) The time evolution of the semiflexible filament dynamics is solved by backward Euler time stepping. This also means that the segment configuration at *the beginning of the time-step* determines the resultant Brownian forces and couples for that time step, and it also determines the directions considered normal and parallel to the segment.

The computational advantage of the above formulation is that many beads are replaced by a single rod as the unit of coarse graining. This reduces the overall size of the equation set and therefore the cost of computing. The formulation also captures the physics of the Brownian bending better: the Euler beam equations are solved without discretizing, the continuous curvature of the filament is reproduced, and filament inextensibility is intrinsically preserved since the θ profile is determined as a function of the segment contour s.

Within the setting of the string-of-rods formulation, the averaged implicit hydrodynamics are incorporated in the following way. First, in the string-of-rods idealization the drag forces along a segment need to be calculated as resultant forces and couple in two mutually perpendicular directions [Fig. 12(b)]. Usually, one of these directions is taken to be along the straight line joining the two segment ends (u_1-), and the other direction is taken along the line perpendicular to it (u_2-) [Fig. 12(b)]. Since our averaged implicit hydrodynamic model is currently only applicable for straight sections of a filament, we use it to determine the resultant drag force and couple over the segment projection u_1-only (Fig. 13). Therefore, *the u_1-projection of a curved segment is equivalent to a "section"* in the averaged implicit hydrodynamics method. We retain the previously described method [6] to determine the resultant drag force and couple in the u_2-projection. The u_2-segment projections are typically much smaller that the u_1-segment projections (much less than 5% for the segment resolutions in the simulations in this paper). Hence, we do not expect the u_2-drag to have a significant effect on the overall segment hydrodynamics. Secondly, the hydrodynamic velocities of the filament ends are also solved for separately. That is, *the filament ends are treated like the end beads of the averaged implicit hydrodynamics method*

FIG. 13. Incorporating averaged implicit hydrodynamics in the string-of-rods idealization of semiflexible filaments. The string-of-rods idealization considers a semiflexible filament (shown in gray) as a continuously curved string of rods or "segments." The average implicit hydrodynamics is used to solve the hydrodynamic velocities of the end beads (circles with solid outlines), and that of the central representative beads (circles with broken outlines) of the u_1-projections of the segments. The u_1-projection of each segment is shown in thin black lines and is along the direction joining the two ends of the segment. Therefore the u_1-projection of each segment constitutes a *section* in the implicit hydrodynamics technique. The hydrodynamic drag force due to the hydrodynamic velocities of an end bead enters the string-of-rods formulation as an end force on that segment. The hydrodynamic drag due to the hydrodynamic velocity of a representative bead enters the string-of-rods formulation as the resultant drag force/couple on the u_1-projection of that segment.

(Fig. 13). The hydrodynamic drag forces arising at the filament ends are treated in the string-of-rods idealization as end forces [6].

The resultant drag force and couple on the u_1-segment projection due to the hydrodynamic velocities of its representative bead are

$$F_i^{kH} = \xi^{sph} v_i^{kH} \frac{L_i^{u1}}{2r} \quad k = n,p, \tag{22}$$

$$F_i^{wH} = \xi^{sph} w_i^{H} \frac{L_i^{u1}}{2r}, \tag{23}$$

F_i^{kH} and F_i^{wH} are the resultant drag force and couple on the u_1-projection of segment i. The superscripts n,p indicate the directions normal and parallel to the u_1-segment projection. v_i^{nH}, v_i^{pH} and w_i^{H} are the normal, parallel and angular hydrodynamic velocities of the representative bead of the u_1-projection of segment i, and L_i^{u1} is the projection of the contour length of segment i in the u_1-direction.

The end force due to the hydrodynamic velocities of the filament ends appear as

$$F_b^{kH} = \xi^{sph} v_b^{kH} \quad k = n,p, \tag{24}$$

where F_b^{kH} is the drag force due to the filament end bead b, and v_b^{nH} and v_b^{pH} are the normal and parallel hydrodynamic velocities of the filament end.

At each time step of the semiflexible filament simulation, the hydrodynamic equations for the representative and end beads are solved simultaneously with the equations for the node degrees of freedom. In keeping with the backward Euler time-stepping solution, all the hydrodynamic interaction terms are calculated based on the filament geometry at the beginning of the time step.
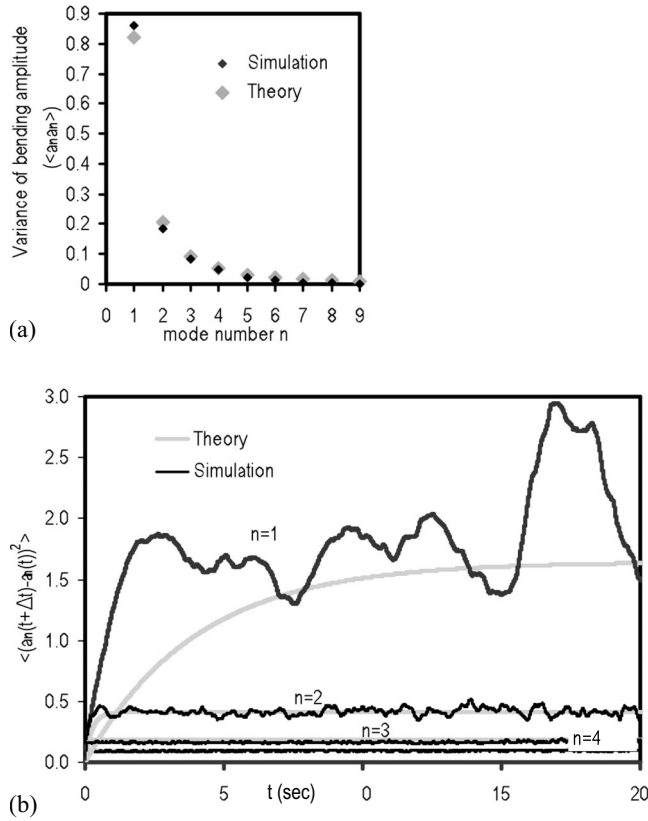
(a)

(b)

FIG. 14. Validation of the rods-on-string idealization of semi-flexible filaments with averaged implicit hydrodynamics. The simulation results for the Brownian fluctuations of a phalloidin-stained actin filament are shown (12 μm length, 7.3e−26 N m^2 persistence length, 0.0025 s simulation time interval). (a) The variances of the amplitude (a_n) of the first nine bending modes (n) are shown. The amplitudes of the bending modes are calculated from the simulation results by decomposing the filament conformation at each time step into Fourier series. Theoretical estimates of the amplitude variances can be made by assuming each bending mode to have $KT/2$ energy (equipartition theorem). The variances determined from the simulation closely match the theoretical estimates. (b) The time evolution of the variance of the bending amplitude for the first four modes is shown in black. Shown in gray are the theoretical estimates of the time evolution obtained by assuming small bending fluctuations and a constant hydrodynamic friction. The simulation results lie in the vicinity of the theoretical estimates.

III. RESULTS AND SIMULATIONS

A. Brownian fluctuations of a semiflexible filament.

We simulated the Brownian fluctuation of a 12 μm phalloidin-stained actin filament with bending stiffness EI =7.3e−26 N m^2, in water at 25 °C [5]. The filament was modeled as a string of 15 segments of length 0.8 μm each, for 25 s in time steps of 0.0025 s. The results of these simulations are shown in Fig. 14. For each time step, the filament contour was decomposed into Fourier sine series and the amplitudes of the first nine Fourier bending modes are calculated [5]. The variance of these bending amplitudes is plotted in Fig. 14(a). The variances compare well against theoretical predictions obtained by equating the bending energy
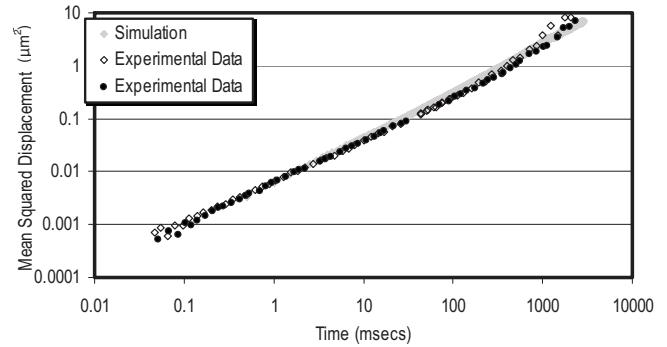

FIG. 15. Experimental validation of model dynamics. The time evolution of the mean-squared displacement of an actin filament is plotted as a function of time interval, Δt. The MSD was determined as $\langle r^2(t\text{-}\Delta t)\rangle$. The simulation result for a 6 μm actin filament is shown with gray diamonds. The experimental observation for homogenously and nonhomogenously labeled actin filaments is shown with unfilled and filled black diamonds, respectively. The experimental data were obtained from Bernheim-Groswasser et al. [24].

of each mode to $KT/2$ (Equipartition theorem) [5,22], validating the Brownian model. We also compare the time evolution of the bending amplitudes of the first four bending modes against that predicted for a semiflexible filament under small bending strains and having a uniform friction coefficient along its length [23]. The plot [Fig. 14(b)] indicates the time evolution behavior to be in the proximity of the theoretical approximation. It also shows that the simulation reaches equilibrium for all the bending modes.

Experimental validation of fluctuation dynamics. Bernheim-Groswasser et al. [24] used fluorescence correlation spectroscopy to measure the time evolution of the mean-squared-displacement (MSD) of fluorescent-labels on actin filaments in Brownian fluctuation, for over five decades in time (20 μs−2 s). They found that only filament fluctuation theories which included hydrodynamic interaction could predict the experimental observations. However beyond 10 ms time intervals, the predictions degraded for the hydrodynamic theories without fitting parameters. We simulated the experiment using actin filament dimensions and experimental conditions reported in the paper [24] (6 μm filament, 17 μm persistence length, 7 nm diameter, and 1 mPa solvent viscosity). We performed the simulation for 10 s at 0.0005 s time intervals. Figure 15 shows the time evolution of the MSD of the filament nodes during the simulation. The simulation data are plotted against the experimental determinations of the MSD of homogenously and nonhomogenously labeled actin filaments. The simulation results compare well against the experimental result, even in time intervals above 10 ms. Note that we did not simulate MSD evolution at time intervals below 0.0005 s.

B. Hydrodynamic screening and Brownian fluctuations of a semiflexible filament

For a preliminary understanding of how hydrodynamic screening and nonuniform friction coefficient affected the Brownian fluctuations of a semiflexible filament, we exam-
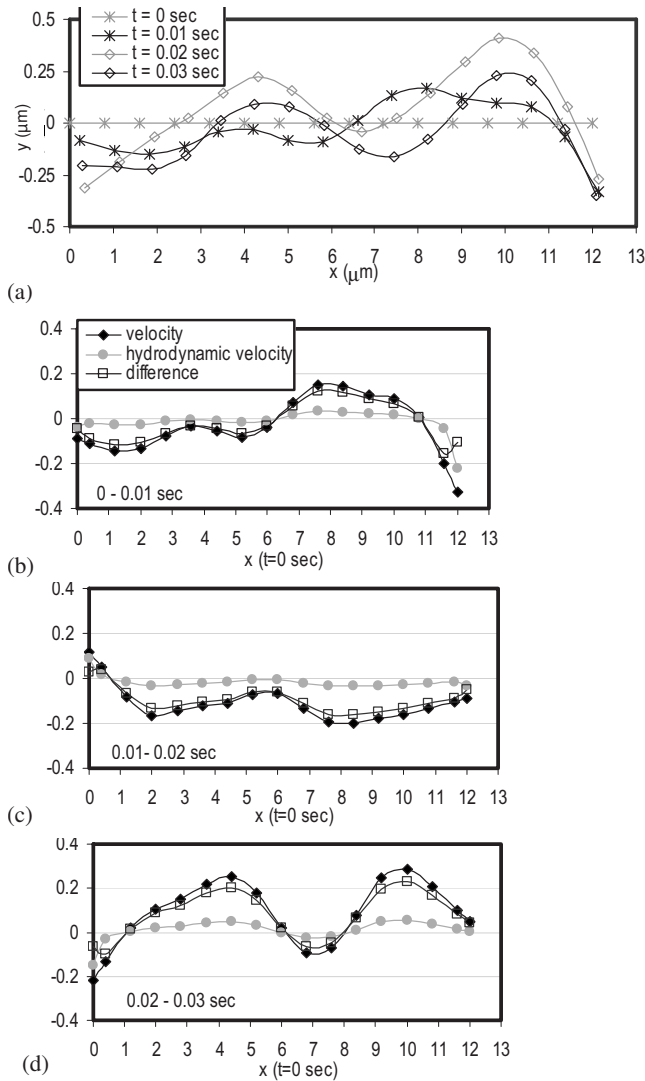
FIG. 16. Hydrodynamic contribution to the Brownian fluctuations of a semiflexible filament. (a) The Brownian conformation of a 12 μm actin filament at 0, 0.01, 0.02, and 0.03 s. The x and y positions of the filament nodes are plotted. (b,c,d) The normal velocities of the end and representative beads in the time intervals of 0–0.01 s (a), 0.01–0.02 s (b), and 0.02–0.03 s (c), plotted against the x positions of the representative/end beads at time $t=0$ s.

ined the contribution of solvent velocity (induced by the bending fluctuations) to the observed velocity along the filament [see Eq. (1)]. Only velocities normal to a segment were considered, although the discussion is applicable to the parallel and rotational velocities as well. We simulate the Brownian fluctuations of the actin filaments at 0.01 sec time steps, and with all other simulation parameters the same as Sec. III A. Shown in Fig. 16(a) are the x/y positions of the filament nodes at the first four simulation times (0, 0.01, 0.02, 0.03 s). The initial conformation of the filament at 0sec is that of a straight rod. We examined the observed and hydrodynamic velocity along the filament at each representative bead and at the end beads for each simulation time interval [Figs. 16(b)–16(d)]. The difference between the observed and hydrodynamic velocities would be the velocity contribution from the induced solvent flow [see Eq. (1)].

In the three time intervals shown, the hydrodynamic velocities are much lower than the observed velocities, except at the filament ends [Figs. 16(b)–16(d)]. Conversely, the solvent velocity profile appears to closely match the observed velocity profile, except at the filament ends. Therefore, the following inductions can be made by comparing the plots in Figs. 16(b)–16(d). The larger hydrodynamic velocities or drag occur at the filament ends. The solvent flow or hydrodynamic screening contributes to a large part of the observed velocity in the interior of the filaments. In fact, the solvent flow contributes to most of the observed velocity at the sides of the convexities in the normal velocity profile [black diamonds in Figs. 16(b)–16(d)], and at points where the hydrodynamic or relative velocity is zero [gray circles in Figs. 16(b)–16(d)]. To the most part, the solvent contribution appears to magnify convexities in the hydrodynamic velocity profiles. These observations suggest that the solvent flow induced by hydrodynamic interactions may have a systematic influence in the Brownian conformations assumed by a semiflexible filament.

C. Confined fluctuations of a semiflexible filament between two stationary filaments

We show that our model captures the lateral hydrodynamic confinement of a fluctuating semiflexible filament between two stationary filaments. We repeat our previous actin filament simulations, but with two stationary actin filaments placed alongside at three confinement widths of 3, 1.5, and 1 μm (Fig. 17). Also, to better capture the confinement we use the central difference instead of the backward time stepping to calculate the hydrodynamic velocities. Calculation of the hydrodynamic velocities requires knowing the relative positions of the filaments. In the backward Euler stepping scheme, the relative positions at the beginning of the time step is used. Using the filament positions at the beginning of the time step may overestimate or underestimate the friction drag experienced by a fluctuating filament, especially if confined. For instance, it would underestimate the drag on a filament approaching a neighbor, leading to crossover. It will also overestimate the drag on a filament moving away from a neighbor, leading to the filament being stuck in the vicinity of the neighbor. Decreasing the simulation time interval would alleviate these issues, but we chose to use the central-difference time stepping instead.

Figure 17 shows the Brownian fluctuations of the 12 μm actin filament between two other stationary actin filaments separated by 3, 1.5, and 1 μm. The filaments undergo fluctuations of decreasing amplitude with increasing confinement. At 1.2 s, the unconfined filament shows a larger translational and rotational diffusion than the confined filaments. These simulation results show that our model is able to capture the two-dimensional confinement of the fluctuating filament that occurs due to hydrodynamic interaction. Moreover, we calculated the variances of the bending amplitude for the different bending modes, for each case of confinement. Figure 18(a) suggests that confinement occurs as a decrease in the amplitude of the bending modes. Figure 18(b) shows the correlation of the contour angles as function of filament
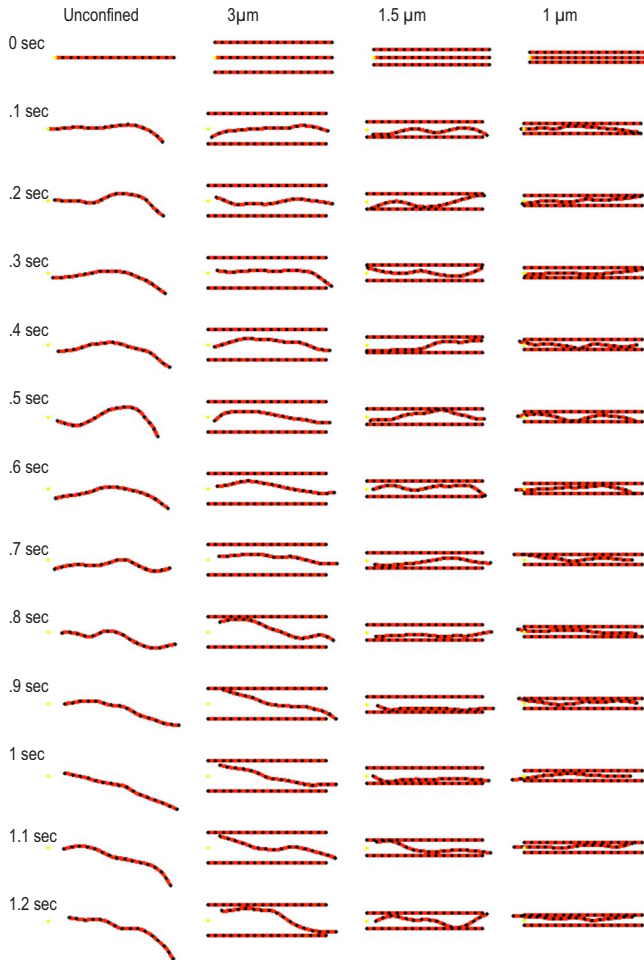
FIG. 17. (Color online) The Brownian fluctuations of a 12 μm actin filament in the unconfined and laterally confined state. The filament properties are similar to that in previous simulations. The simulations were performed in time intervals of 0.0025 s. The confined filament fluctuates between two other stationary filaments separated by 3, 1.5, and 1 μm (from the left to right in figure). From top to down, the fluctuations of the filament at every 0.1 s intervals are shown. The filament conformation is obtained by fifth-order interpolation between the filament nodes (shown as black dots). The filament contour length between two nodes (black dots) is 0.8 μm.
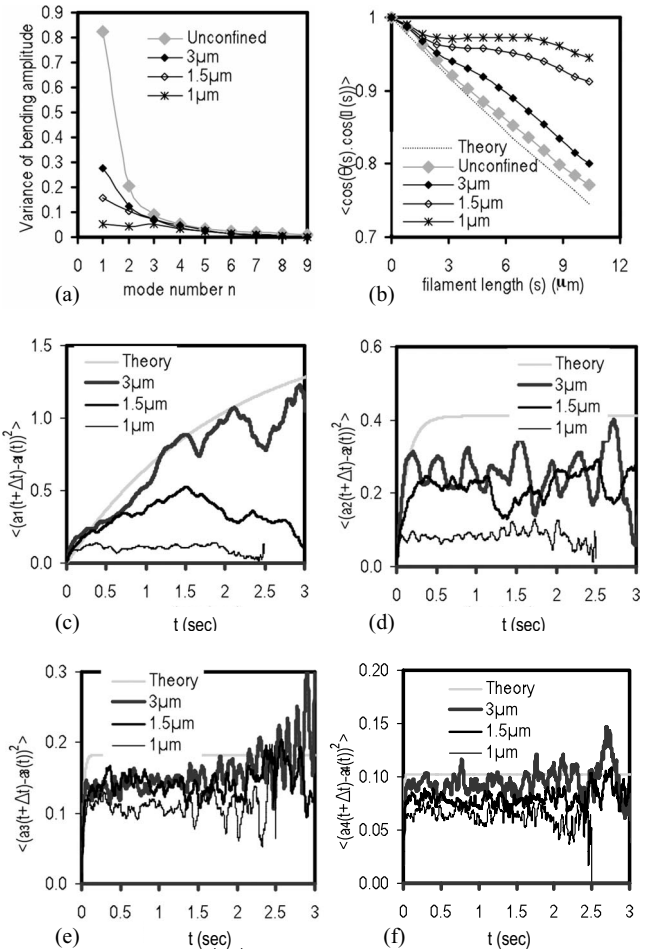

FIG. 18. Dynamics of laterally confined fluctuating actin filaments. (a) Variance of the first four bending amplitudes for different degrees of confinement. (b) Angle correlation along the filament length for different degrees of confinement. (c) Time correlation of the amplitude of the first bending mode (a_1) for different degrees of confinement. (d) Time correlation of the amplitude of the second bending mode (a_2) for different degrees of confinement. (e) Time correlation of the amplitude of the third bending mode (a_3) for different degrees of confinement. (f) Time correlation of the amplitude of the fourth bending mode (a_4) for different degrees of confinement.

length. The decay in correlation along the filament contour is much slower with increasing confinement, and the overall degree of correlation is higher with increasing confinement. The angle correlation profiles suggest that the filament persistence length increases with increasing confinement [Fig. 18(b)]. A similar increase in persistence length was observed by Koster *et al.* [25] for actin filaments fluctuating in confining microchannels of decreasing width. Figures 18(c)–18(f) show the time correlation profile of the first four bending modes for the different degrees of confinement. While the plots clearly show the equilibrium bending variance to decrease with increasing confinement, we do not have conclusive data yet on how the time relaxation for bending changes with confinement.

IV. SUMMARY AND DISCUSSION

Semiflexible filaments, constituting the chief structural ingredients of the cytoskeleton [26] while contributing to the mechanical signaling pathways in the cell [27,28], are generally subject to hydrodynamic forces due to solvent flows induced by the bending and diffusive motions within the filaments themselves and from their surrounds filaments. The aim of this paper was to include the effect of hydrodynamic interaction in a dynamic model of semiflexible filament. The drag along a filament is altered by the solvent flow induced by the bending and diffusive motions along the filament, and along neighboring filaments. For example, the drag along a rigid filament in uniform motion is not uniform due to the hydrodynamic screening within the filament. The nonuniform drag would have caused a semiflexible filament to

bend. Therefore, hydrodynamic interactions do not only affect the bending fluctuations of a filament in nondilute systems, but also affect filaments in dilute systems due to the altered drag from hydrodynamic screening effects. It is therefore important for realistic models of semiflexible filaments dynamics to include hydrodynamic interaction.

Due to the induced solvent flow, the true relative velocity along the filament is different from the observed velocity. We refer to the true relative velocity along the filament as the hydrodynamic velocity. The common way to capture the relative velocities along the filament is to idealize it as a string-of-beads, and use the linearity of Stokes flow to determine the induced solvent field by superposing the separate solvent fields due to each bead. However, the first-order Stokes superposition neglects the back reflection of solvent flow. We corrected for this by casting the true relative velocity of the bead as a new variable and solving for it implicitly. We call the true relative velocity of the bead as its hydrodynamic velocity. The one-step implicit solving of hydrodynamic variables is equivalent to infinite superpositions of the bead solvent fields or infinite reflections in the Method of Reflections because (1) each superposition serving to enforce the no-slip boundary condition at a bead can be mathematically interpreted as requiring that solvent flow be induced by the hydrodynamic velocity of a particle alone, (2) infinite orders of explicit iteration are equivalent to one implicit solution. The predictions of the implicit technique deteriorate at very small distances between beads. This is not because of the Stokesian superpositions, but because the presence of a bead in the solvent is represented by a point perturbation in the velocity field. In other words, the equations for the solvent flow around a bead (Fig. 2) do not respect the impenetrability of the bead. However, in spite of this limitation, the predictions of an implicit or infinite-order superposition is vastly superior to that of a first-order superposition, especially in that it captures the hydrodynamic influence of stationary particles while being relatively easy to implement.

A string-of-beads approach is traditionally limited by the computational size of even modeling a single filament. The proposed method addresses this limitation by assuming sections of beads, excepting the beads at the ends of filaments, to have the same average hydrodynamic velocities. We do not include the end beads in the averaging because the larger hydrodynamic drags are typically concentrated at the filament ends. By solving for their relative velocities separately, we are able to better resolve the hydrodynamic profile along the filament. The averaging is performed by approximating the normal and parallel hydrodynamic velocities of the beads in a section by the normal, parallel, and angular hydrodynamic velocity of the central representative bead in the section. This is equivalent to approximating the hydrodynamic profile in the section by a linear normal hydrodynamic profile and a constant parallel hydrodynamic profile. As a result of such averaging, the hydrodynamic equations need to be only solved for the representative equations, but the hydrodynamic influence from all beads is included. We do not write the equations for the angular hydrodynamic velocity of the representative bead in a form similar to its normal hydrodynamic velocity. Doing so would result in the equations being trivially zero. Instead we write the angular hydrody-

namic equation as a differential of the representative bead's normal hydrodynamic velocity equation. In other words, we solve for the angular hydrodynamic velocity by differentiating normal hydrodynamic velocity profile of the section, at the representative bead.

We incorporated the averaged implicit hydrodynamics into an earlier proposed string-of-rods idealization of a semiflexible filament [6]. In that formulation, the semiflexible filament is divided into continuously curved segments. The drag force distributed along on a curved segment is resolved into resultant forces and couples acting on two mutually perpendicular projections of the segment. One projection (u_1-) is taken to be the line joining the segment ends. We treat this projection as equivalent to a "section" in the averaged implicit technique. The hydrodynamic velocity of the central representative bead of the projection is used to determine the resultant drag forces and couple on it. The hydrodynamic equations of the filament end beads and the hydrodynamic equations of the representative beads of the u_1-projections are solved simultaneously with the equations of the string-of-rods idealization. We found that the time evolution of the bending amplitudes lies in the vicinity of the theoretical approximation. The theoretical approximation assumes that the filament bending is small and that the friction coefficient along the filament is uniform, i.e., it neglects hydrodynamic interaction. We also simulated experimental data on the time evolution of the mean-squared displacement (MSD) of fluctuating actin filaments. A good prediction was observed even for time intervals above 10 ms, where models of transverse filament fluctuation, hydrodynamic interaction included, fared less well [24]. The time evolution of the filament MSD, observed in the experiment and in our simulation, was much larger than the predictions of filament models with no hydrodynamic interaction. This suggests that hydrodynamic interaction could possibly decrease the time-relaxation constants for the bending of semiflexible filaments.

Examination of the contribution of hydrodynamic forces to the bending fluctuations of a semiflexible filament showed that at point along the filament, the difference between the observed and hydrodynamic velocity gives the part of the point's motion that occurs from drifting in the solvent flow induced by its neighbors. We found that a large part of the observed velocities along a filament can be attributed to drifting in induced solvent flow. And as expected, the observed velocities at the filament ends received much less contribution from the induced solvent flow. Thus the hydrodynamic drag profiles along the fluctuating semiflexible filament are reminiscent of those observed along rigid filaments {see Fig. 5(a) and Ref. [7]}, except that the nonuniformities are less pronounced. This is because a semiflexible filament can bend to equalize the nonuniform drag forces along it. More study is required to understand how hydrodynamic interactions systematically affect the bending fluctuations of a semiflexible filament.

We tested the ability of our model to show the confinement of a fluctuating filament between neighboring filaments due to hydrodynamic interaction. For ease of demonstration, we chose the neighboring filaments to be stationary. We note that a first-order superposition would miss the hydrodynamic confinement from stationary filaments. In order to capture

the fast-changing drag on a confined filament as it moves toward and away from its neighbors, we chose to solve the hydrodynamic equations alone by central-difference time stepping instead of the backward time stepping used in the rest of the model. A central time stepping takes the average of the filament positions at the beginning and end of the time step, and therefore gives a better estimate of the average drag experienced by the filament during the simulation time interval. The simulation results show the persistent length of the filament increases with increasing confinement, suggesting that the filament confinement occurs as change in persistence length. We also show the time evolution of the bending amplitudes of the confined filaments that was observed in our simulations. More rigorous studies are required, however, to quantify the time-relaxation behavior. Finally we note that the crossing over of filaments is not prevented in our simulations. Since the hydrodynamic equations are only solved at representative and end beads and since the hydrodynamic forces only increase by r^{-1} as the r (distance of separation) decreases, the filament is free to crossover each other. The simulations only break down when the representative or end beads intersect. Accounting for the van der Waals steric hindrance forces would alleviate this problem to a large extent. However, we chose not to include the steric forces in our two-dimensional model, because a two-dimensional (2D) approximation of a three-dimensional (3D) system by itself tends to overestimate the confinement effect.

To conclude, we presented a model of semiflexible filaments that accounts for the hydrodynamic effects originating both within itself and from interaction with its neighbors. The model offers great potential for understanding the rheology of *nondilute* semiflexible filament systems, which in turn is useful for understanding the mechanics of cell and tissue matrices [26].

[1] E. Frey, K. Kroy, and J. Wilhelm, e-print arXiv:cond-mat/9808022.

[2] J. Howard, *Mechanics of Motor Proteins and the Cytoskeleton* (Sinauer Associates, Sunderland, MA, 2001).

[3] R. Everaers, F. Jülicher, A. Ajdari, and A. C. Maggs, Phys. Rev. Lett. **82**, 3717 (1999).

[4] M. Alberto, C. M. David, and P. Matteo, J. Chem. Phys. **122**, 084903 (2005).

[5] F. Gittes, B. Mickey, J. Nettleton, and J. Howard, J. Cell Biol. **120**, 923 (1993).

[6] P. L. Chandran and M. R. K. Mofrad, Phys. Rev. E **79**, 011906-1 (2009).

[7] M. C. Lagamarsino, I. Pagonabarraga, and C. P. Lowe, Phys. Rev. Lett. **94**, 148104 (2005).

[8] A.-K. Tornberg and K. Gustavsson, J. Comput. Phys. **215**, 172 (2006).

[9] S. Yamamoto and T. Matsuoka, J. Chem. Phys. **102**, 2254 (1995).

[10] J. Happel and H. Brenner, *Low Reynolds Number Hydrodynamics, with special applications to particulate media* (Springer New York, New York, 1991).

[11] R. L. Panton, *Incompressible Flow*, (John Wiley and Sons, Canada Ltd., Hoboken, NJ, 1997).

[12] J. Happel, (Martinum Nijoff Publishers, The Hague, The Netherlands, 1983).

[13] H. Brenner, J. Fluid Mech. **12**, 35 (1962).

[14] M. J. Gluckman, R. Pfeffer, and S. Weinbaum, J. Fluid Mech. **50**, 705 (1971).

[15] S. Wakiya, J. Phys. Soc. Jpn. **22**, 1101 (1967).

[16] H. Faxen, Z. Angew. Math. Mech. **7**, 79 (1927).

[17] J. Happel and R. Pfeffer, AIChE J. **6**, 129 (1960).

[18] G. H. Zheng, R. L. Powell, and P. Stroeve, Chem. Eng. Commun. **117**, 89 (1992).

[19] S. Broersma, J. Chem. Phys. **74**, 6989 (1981).

[20] G. Li and J. X. Tang, Phys. Rev. E **69**, 061921 (2004).

[21] E. Swanson and D. C. Teller, J. Chem. Phys. **72**, 1623 (1980).

[22] J. Kas, H. Strey, J. X. Tang, D. Finger, R. Ezzell, E. Sackmann, and P. A. Janmey, Biophys. J. **70**, 609 (1996).

[23] C. P. Brangwynne, G. H. Koenderink, E. Barry, Z. Dogic, F. C. MacKintosh, and D. A. Weitz, Biophys. J. **93**, 346 (2007).

[24] A. Bernheim-Groswasser, R. Shusterman, and O. Krichevsky, J. Chem. Phys. **125**, 084903 (2006).

[25] S. S. D. Koster and T. Pfohl, J. Phys. Condens. Matter. **17**, S4091 (2005).

[26] *Cytoskeletal Mechanics: Models and Measurments*, edited by M. R. K. Mofrad and R. D. Kamm (Cambridge University Press, Cambridge, U.K., 2006).

[27] *Cellular Mechanotransduction: Diverse Perspectives from Molecules to Tissues*, edited by M. R. K. Mofrad and R. D. Kamm (Cambridge University Press, Cambridge, U.K., 2009).

[28] G. Bao, R. D. Kamm, W. Thomas, W. Hwang, D. A. Fletcher, A. J. Grodzinsky, C. Zhu, and M. R. K. Mofrad, Cellular and Molecular Bioengineering (to be published).